Two-photon optics of Bessel-Gaussian modes

Melanie McLaren,[1,2] Jacquiline Romero,[3] Miles J. Padgett,[3] Filippus S. Roux,[1] and Andrew Forbes[1,2,*]
[1]*CSIR National Laser Centre, P.O. Box 395, Pretoria 0001, South Africa*
[2]*Laser Research Institute, University of Stellenbosch, Stellenbosch 7602, South Africa*
[3]*Department of Physics and Astronomy, SUPA, University of Glasgow, Glasgow, United Kingdom*
(Received 12 June 2013; published 9 September 2013)

In this paper we consider geometrical two-photon optics of Bessel-Gaussian modes generated in spontaneous parametric down-conversion of a Gaussian pump beam. We provide a general theoretical expression for the orbital angular momentum (OAM) spectrum and Schmidt number in this basis and show how this may be varied by control over the radial degree of freedom, a continuous parameter in Bessel-Gaussian modes. As a test we first implement a back-projection technique to classically predict, by experiment, the quantum correlations for Bessel-Gaussian modes produced by three holographic masks: a blazed axicon, a binary axicon, and a binary Bessel function. We then proceed to test the theory on the down-converted photons using the binary Bessel mask. We experimentally quantify the number of usable OAM modes and confirm the theoretical prediction of a flattening in the OAM spectrum and a concomitant increase in the OAM bandwidth. The results have implications for the control of dimensionality in quantum states.

DOI: 10.1103/PhysRevA.88.033818 PACS number(s): 42.50.Tx, 03.65.Ud, 02.30.Gp, 42.40.Jv

I. INTRODUCTION

Quantum entanglement has formed the basis of several quantum information technologies, including quantum computing and quantum communication. Such examples include quantum ghost imaging [1], quantum cryptography [2,3], and quantum computing algorithms [4]. The amount of information in an entangled state depends on the dimension of its associated Hilbert space. Photonic quantum information is often encoded in photon polarization, which is constrained in a two-dimensional Hilbert space. In contrast, the spatial degrees of freedom (transverse spatial modal profile) of a photon span an infinite-dimensional Hilbert space. Researchers are therefore focusing on the spatial modes of paraxial optical beams to increase the information capacity per photon. To this end, the most commonly used basis is that of the Laguerre-Gaussian (LG) modes.

It was shown that the LG modes are orbital angular momentum (OAM) eigenstates of photons [5]. Each photon in such a beam carries an amount of OAM equal to $\ell\hbar$, where ℓ is the azimuthal index of the LG mode. OAM is conserved in spontaneous parametric down-conversion (SPDC); this has been demonstrated both theoretically [6,7] and experimentally [8]. The implication thereof is that a pair of down-converted photons is naturally entangled in terms of the OAM eigenstates. The LG modes are often approximated to include only the azimuthal phase term, hence they are also called helical modes. The radial components of the LG modes are often ignored, as they require complex amplitude modulation (intensity masking) [9].

By approximating the phase-matching condition with a Gaussian function, it was shown [10] that the Schmidt basis for the quantum state produced in SPDC is the LG modes; that is, the Schmidt basis is a basis of OAM eigenstates. Without this approximation, the LG modes are still close to being the Schmidt basis [10,11]. Thus, the LG modes are entangled not only in the azimuthal index, but also in terms of the radial index [12]. High-dimensional entanglement is dependent on the number of usable OAM modes in the state [13]. However, the experimental parameters (e.g., mode size of single-mode fiber) involved in the detection of the spectrum of helical modes place restrictions on the control one has over the bandwidth of OAM components in the entangled state.

The LG modes are not the only OAM basis. Higher-order Bessel beams [14,15] and Bessel-Gaussian (BG) beams [16] also have helical wavefronts and carry OAM. The spatial modal bases are related by unitary transformations such that the down-converted quantum states are also entangled in terms of the BG modes. The entangled BG modes [17,18] allow for additional control over quantum state preparation, as they have a continuous radial scale parameter that distinguishes different modes, instead of a discrete radial index as in LG modes.

In this paper we outline experimentally and theoretically how the BG modes may be used to increase the dimensionality of entangled states. To do so we provide a thorough description of the two-photon "geometric optics" [1] of BG modes entangled in the OAM basis. We use classical back-projection as an experimental tool to study BG projective measurements and show that we are able to predict the strength of the coincidence correlations in the entanglement experiment. We quantify the number of measurable OAM modes by calculating the Schmidt number and demonstrate a clear dependence of the dimensionality on the radial component, in agreement with theory.

II. THEORY

The probability that the biphoton quantum state after the SPDC process will contain a particular measurement state $\rho_{\mathrm{m}} = |\Psi_s\rangle|\Psi_i\rangle\langle\Psi_s|\langle\Psi_i|$ is given by the trace $\mathrm{Tr}\{\rho\rho_{\mathrm{m}}\} = |\mathcal{M}|^2$, where $\mathcal{M}$ is the scattering amplitude. For a monochromatic paraxial pump, with signal and idler beams in a degenerate collinear SPDC process with type I phase matching, the

*aforbes1@csir.co.za

scattering amplitude is given by [11]

$$\mathcal{M} = \Omega_0 \int M_s^*(\mathbf{K}_1) M_i^*(\mathbf{K}_2) M_p(\mathbf{K}_1 + \mathbf{K}_2) \times P(\Delta k_z) \frac{d^2k_1}{(2\pi)^2} \frac{d^2k_2}{(2\pi)^2}, \quad (1)$$

where $M_s(\mathbf{K})$, $M_i(\mathbf{K})$, and $M_p(\mathbf{K})$ are the Fourier spectra of the two-dimensional mode profiles for the signal, idler, and pump beams, respectively; $\mathbf{K}$ represents the coordinate vector in the two-dimensional transverse Fourier domain; Ω_0 is a constant that determines the overall conversion efficiency; and $P(\Delta k_z)$ is a function that represents the phase-matching condition.

The phase-matching condition is given in terms of a sinc function,

$$P(\Delta k_z) = \mathrm{sinc}\left(\frac{\Delta k_z L}{2\pi}\right) = \mathrm{sinc}(\zeta\, |\mathbf{K}_1 - \mathbf{K}_2|^2), \quad (2)$$

where

$$\zeta = \frac{n_o \lambda_p L}{8\pi^2}, \quad (3)$$

with n_o being the ordinary refractive index of the nonlinear crystal, λ_p being the wavelength of the pump and L being the crystal length. Assuming that the pump wavelength is much smaller than any of the other dimension parameters, the width of the sinc function in Eq. (3), as determined by $\zeta^{-1/2}$, is much larger than the widths of the angular spectra of the pump, signal, or idler beams [13]. Hence, one can approximate $P = 1$ and the Fourier integral in Eq. (1) can be transformed into a spatial domain given by

$$\mathcal{M} = \Omega_0 \int m_s^*(\mathbf{x}) m_i^*(\mathbf{x}) m_p(\mathbf{x}) d^2x, \quad (4)$$

where $m_s(\mathbf{x})$, $m_i(\mathbf{x})$, and $m_p(\mathbf{x})$ are the two-dimensional mode profile functions for the signal, idler, and pump beams, respectively. The pump beam has a mode profile described by a Gaussian function, which is expressed as

$$m_p = \frac{1}{\omega_0}\sqrt{\frac{2}{\pi}} \exp\left[-\frac{(x^2+y^2)}{\omega_0^2}\right], \quad (5)$$

where the radius of the mode profile of the pump beam is given by ω_0. We consider the case where the signal and idler beams are BG modes with azimuthal indices ℓ and $-\ell$, respectively, and with scaling parameters k_{r1} and k_{r2}, respectively. For simplicity we assume that $k_{r1} = k_{r2} = k_r$. A BG mode with a specific ℓ value is produced by evaluating the following integral:

$$M_\ell^{\mathrm{BG}} = \frac{1}{2\pi}\int_0^{2\pi} \mathcal{G} \exp(-i\ell\beta)\, d\beta. \quad (6)$$

The generating function, $\mathcal{G}$ for BG modes at $z = 0$ is then given by

$$\mathcal{G} = \sqrt{\frac{2}{\pi}}\frac{1}{\omega_1} \exp\{ik_r[y\cos(\beta) - x\sin(\beta)]\} \times \exp\left[-\frac{(x^2+y^2)}{\omega_1^2}\right], \quad (7)$$

where the radius of the Gaussian envelope of the mode is ω_1 and β is an angular generating parameter.

The coefficients for any given value of the azimuthal index ℓ (with opposite signs for the signal and idler beams, respectively) can be extracted by substituting Eqs. (5) and (7) into Eq. (4) and solving the integral. The OAM spectrum, represented by these coefficients, is given by

$$C_\ell = (-1)^\ell \sqrt{\frac{2}{\pi}} \frac{2\Omega_0\omega_0^2}{2\omega_0^2 + \omega_1^2} \times \exp\left[\frac{-k_r^2\omega_1^4}{4(2\omega_0^2+\omega_1^2)}\right] \frac{I_\ell\left[\frac{k_r^2\omega_0^2\omega_1^2}{2(2\omega_0^2+\omega_1^2)}\right]}{I_\ell\left[\frac{k_r^2\omega_1^2}{4}\right]}, \quad (8)$$

where $I_\ell(\cdot)$ is the modified Bessel function of the first kind [19]. The equivalent coefficients in the helical basis, for zero radial index, are given by

$$C_\ell = \Omega_0\sqrt{\frac{2}{\pi}}\left(\frac{2\omega_0^2}{2\omega_0^2+\omega_1^2}\right)^{|\ell|+1}. \quad (9)$$

An estimate of the OAM bandwidth of this spectrum can be calculated by computing the azimuthal Schmidt number [10] given by

$$K = \frac{\left(\sum_\ell C_\ell^2\right)^2}{\sum_\ell C_\ell^4}. \quad (10)$$

In the case where the OAM spectrum is computed in terms of the BG modes, one cannot obtain a closed form expression for the azimuthal Schmidt number. However, one can compute the azimuthal Schmidt number numerically from the analytical result in Eq. (8) for any given value of k_r. Figure 1 shows the OAM spectra for the helical and BG modes. In the case where Eq. (2) is not approximated as 1, the OAM spectra are partly determined by the length of the nonlinear crystal [20].

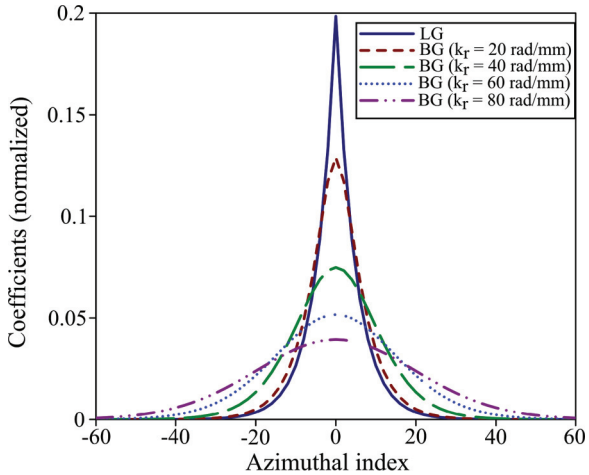

FIG. 1. (Color online) Comparison of the OAM spectra for the helical modes ($k_r = 0$) and BG modes ($k_r = 20,40,60,80$ rad/mm) using Eqs. (9) and (8), respectively, with $\omega_0 = 0.5$ mm and $\omega_1 = 0.23$ mm. The number of usable OAM modes increases with the radial wavevector k_r.

III. SIMULATION OF SPATIAL ENTANGLEMENT WITH CLASSICAL LIGHT

There has been a great deal of interest in mathematically determining a method to predict quantum correlations with particular reference to quantum communication and imaging [21–24]. The measurable correlation of the entangled photons in a typical SPDC experiment depends on the quality of state generation (e.g., the range of OAM states that SPDC actually produces) and state detection (e.g., the range of OAM states that can be detected by the measurement scheme). It is useful to isolate the effect of generation from detection, and vice versa. We are interested in investigating the quality of our detection system, and to this end, we introduce a back-projection experiment inspired by the advanced-wave representation of Klyshko [25].

The Klyshko picture is useful in assessing the conditional probability distribution—the probability of detecting a photon at detector B given that another photon is detected at detector A. Klyshko considered the field detected in arm A as propagating in reverse back to the crystal plane, where it reflects off the crystal to propagate forward through the system to detector B. Using this picture and geometrical optics arguments, the two-photon correlations measured in SPDC can be predicted, as in the ghost imaging and two-photon optics experiments in [1] and [21]. More than a theoretical tool, the Klyshko picture can also be applied experimentally. One of the detectors can be replaced with a classical light source and propagated through one arm back onto the crystal plane, where a mirror has been placed (this corresponds to the wave propagating in reverse). At the crystal, this back-projected beam is reflected and propagated forward onto the components of the other arm and onto the other detector. The number of photons registered by this detector can be optimized to ensure the stringent alignment required by the system and, more importantly, can be used to predict the expected behavior of the two-photon correlation. With these in mind, we implemented a back-projection experiment. Figure 2(a) shows a simple schematic of an entanglement setup. Because we are interested in measuring spatial transverse profiles, we use a spatial light modulator (SLM), which consists of a liquid crystal display onto which computer-generated holograms are encoded. SLMs allow arbitrary phase transformations to be performed on an incident beam, work in both the single-photon (as in SPDC) and the classical (as in back-projection) regimes, and have been useful in the demonstration of state tomography [26]. The entangled state is generated at the nonlinear BBO crystal, then projected into a particular spatial mode using SLMs, and, finally, detected by single-photon detectors. A more detailed description of the entanglement setup is given in Sec. V.

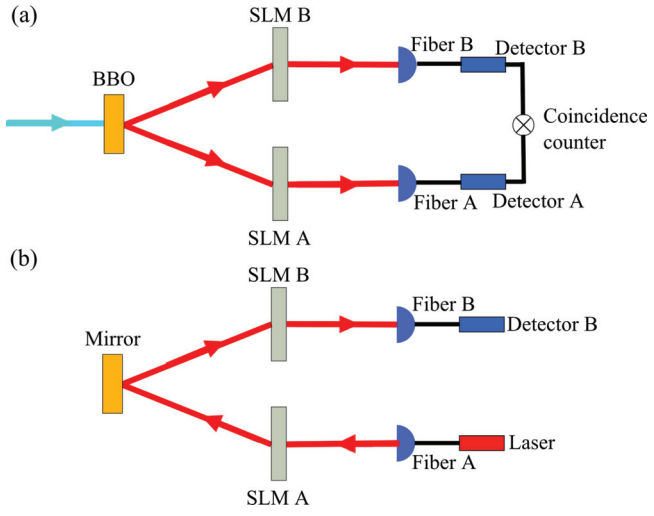

FIG. 2. (Color online) (a) Schematic of an entanglement setup. The entangled photon pairs were generated by the BBO crystal, the combination of the SLMs and detectors projected the photon pair into a particular state, and the detection of the pairs was measured with a coincidence counter. (b) Back-projection schematic, where the BBO crystal is replaced with a mirror such that SLM A is imaged onto SLM B (imaging details are given in Sec. V). Light from a 710-nm diode laser was coupled into fiber A, whereafter it was imaged to SLM A, followed by SLM B, and then recoupled into fiber B. By placing a CCD camera at the plane of the mirror (BBO crystal), we guarantee that we are measuring BG fields.

Figure 2(b) illustrates the changes made to Fig. 2(a) in order to perform back-projection measurements. A 710-nm diode laser with a Gaussian profile replaced detector A and was connected to fiber A. The output was imaged through the system to SLM A, which was then imaged onto a mirror at plane of the crystal (all imaging systems are specified in Sec. V). From here, the light was imaged onto SLM B, and SLM B is in turn imaged onto the facet of single-mode fiber B. The fiber was coupled to detector B, which registered the single-photon count rate. Figure 2(b) shows only a schematic of the back-projection experiment, however, the full details, including lenses and apertures, are given in Sec. V. In order to have significant single-photon counts, in the context of the spatial modes, which we are trying to measure, maximum coupling of the light from fiber A to fiber B occurs when the transmission functions encoded on the SLMs are phase conjugates of each other. These patterns should ensure the fundamental mode from fiber A is coupled into fiber B. To illustrate this, if a positive lens function with focal length f_1 is encoded onto SLM A, a negative lens function with focal length f_2 must be encoded onto SLM B to produce a Gaussian mode, which can only then be coupled into fiber B. When $f_1 = -f_2$ the transverse and angular positions of the initial and final beams remain the same. However, identical focal lengths result in a change in the angular position, producing a divergent beam at fiber B and thus reducing the coupling efficiency.

IV. BACK-PROJECTION RESULTS

OAM entanglement is typically measured in the LG basis by encoding only the azimuthal phase term onto an SLM, described by the transmission function,

$$T(\phi) = \exp(i\ell\phi), \tag{11}$$

where ϕ is the azimuthal angle. Depending on the azimuthal index ℓ an incoming Gaussian mode is transformed into an approximated LG mode carrying the OAM of $\ell\hbar$ per photon. This is only an approximation, as the radial dependence of

the LG function has been neglected in favor of efficiency [11,12]. By selecting the BG basis in which to measure OAM entanglement, we have access to a continuous scaling parameter for the radial component of the BG modes. We consider blazed axicons, which have been well documented for producing BG beams, binary axicons, and binary Bessel functions.

A. Blazed axicon

The first phase pattern investigated was that of an axicon described by a blazed (kinoform element) function, first described by Turunen *et al.* [27]. The conversion from Gaussian to BG mode was performed using the phase-only hologram of an axicon described by the transmission function

$$T_1(r,\phi) = \exp(ik_r r)\exp(i\ell\phi), \tag{12}$$

where k_r is the radial wave vector and ℓ is the azimuthal index. The number of rings of the BG beam increases with k_r. A blazed grating is added to separate the diffraction orders so that this kinoform diffracts approximately 100% of the incoming light into the first diffraction order. Figure 3(a) shows an example of such a phase pattern for $k_r = 21$ rad/mm and $\ell = 1$. By placing a CCD camera (aligned to the first diffraction order) in the plane of the crystal, we were able to view the mode at this plane, corresponding to the detected mode. The shape of the beam imaged from the SLM (blazed axicon) for $k_r = 21$ rad/mm and $\ell = 1$ is shown in Fig. 3(b). Figure 3(c) shows the experimental measurements of the single counts measured at detector B. The counts recorded show a strong correlation along the diagonal corresponding to values of k_r

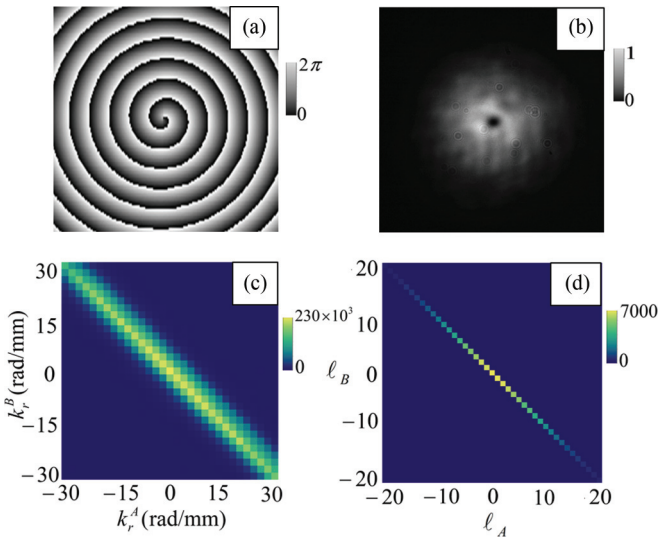

FIG. 3. (Color online) (a) Phase pattern used to define an axicon of $k_r = 21$ rad/mm and $\ell = 1$. (b) CCD image of a BG beam generated from a blazed axicon function of $k_r = 21$ rad/mm and $\ell = 1$ at the plane of the crystal. (c) Density plot of the single count rates measured in back-projection for different blazed axicon phase patterns; varying k_r with $\ell = 0$. (d) Density plot of the single count rates measured in back-projection for a particular blazed axicon; $k_r = 21$ rad/mm and varying ℓ.

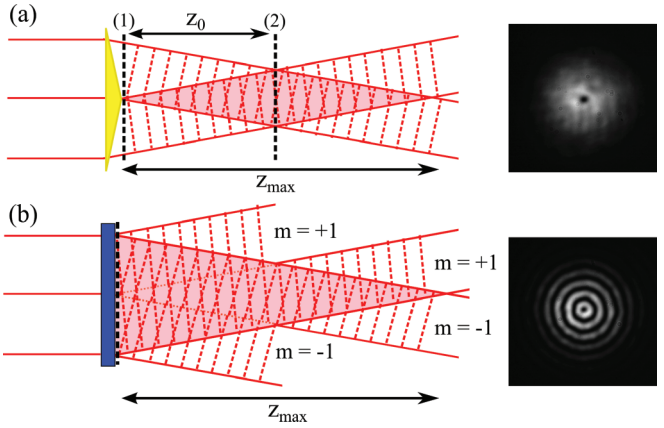

FIG. 4. (Color online) (a) Formation of a Bessel-Gaussian (BG) beam by directing a Gaussian beam on a standard axicon. No rings are seen in the plane of the dotted line (1) (corresponding to the plane immediately after the SLM), as the BG beam has not yet formed. At plane (2) the interfering plane waves produce a well-defined BG beam after propagating a distance z_0. (b) Formation of a BG mode by directing a Gaussian beam on a binary axicon. A BG-like beam is observed immediately after the SLM due to the interference of the diffraction orders, $m = \pm 1$, of the binary hologram.

of equal magnitude but opposite sign. The single count level was significant only when the system consisted of a positive radial wave vector k_r on one SLM with the corresponding negative radial wave vector $-k_r$ on the other (although the radial wave vector is a positive entity, we assign a negative value to k_r to represent the conjugate phase). This translates to a positive axicon imaged onto a negative axicon, to produce a Gaussian beam, which is analogous to the lens functions discussed in Sec. III. As k_r is a continuous variable, we expected a gradual decrease in the count rate moving away from the diagonal elements. The OAM correlations for a particular blazed axicon function are shown in Fig. 3(d). We note that the recorded mode [Fig. 3(b)] does not exhibit a well-defined BG beam, since this is only fully formed (maximum number of rings) at a distance z_0 after the SLM (blazed axicon). This is more clearly illustrated in Fig. 4(a), where we depict an axicon illuminated with a Gaussian beam, analogous to the back-projected light from the fiber (Gaussian source) illuminating the SLM (axicon). Immediately after the axicon the conical waves have not sufficiently overlapped to create a Bessel beam, so plane (1) is a Gaussian-like beam. If a spiral phase is added to the axicon, then one observes a Gaussian-like beam with a central null, as shown in the adjacent inset. Only at plane (2), where the interfering conical waves overlap completely, would a BG beam with a maximum number of rings be generated. However, this is some distance from the axicon. The implication is that when the SLM is programmed with a blazed axicon, and this plane is imaged to the crystal, one can never detect true BG modes.

B. Binary axicon

One can question whether the OAM modes are truly measured in the BG basis with a blazed axicon, as the image at the crystal plane did not resemble a Bessel beam. This issue

can be remedied by using a different approximation to an axicon function. That is, the second phase pattern studied also incorporated the axicon function, but as a binary function,

$$T_2(r,\phi) = \mathrm{sgn}\{\exp(ik_r r)\}\exp(i\ell\phi), \tag{13}$$

where $\mathrm{sgn}\{z\} = z/|z|$. The kinoform used to approximate an axicon in the previous sub-section was replaced with a two-level binary approximation. The efficiency of a kinoform DOE into the first diffraction order is almost 100%, while the efficiency of a binary function is about half that; 42% in both the $m = \pm 1$ diffraction orders. This effect has an advantage in that a Bessel-like beam forms immediately after the SLM. Figure 4(b) illustrates a Gaussian beam incident on an SLM encoded with the binary axicon function described in Eq. (13). The binary axicon hologram deflects both diffraction orders symmetrically such that the plane waves interfere with each other and produce a Bessel-like region immediately after the SLM, i.e., at $z_0 = 0$. This results in a well-defined BG mode directly after the SLM, shown in the inset in Fig. 4(b). By filtering the higher diffraction orders using a variable aperture (see experimental setup in Sec. V), a clear image of a BG mode was recorded at the crystal plane; see Fig. 5(b).

Similarly to the previous case, an incoming Gaussian beam can be converted into a mode with a radial wave vector of either k_r or $-k_r$. The recorded single count rate shown in Fig. 5(c) illustrates a distinct difference between the blazed and the binary axicon functions. The binary function on SLM A transforms the incoming Gaussian mode into a BG mode with radial wave vector of either k_r or $-k_r$, such that there is an equal probability of generating a photon with a positive or a negative k_r value. Subsequently SLM B, encoded with the same function, is also able to convert both BG modes (with wave-vector components k_r and $-k_r$) into a Gaussian mode. As a result, single count rates were observed for $k_r^A = k_r^B$ and $k_r^A = -k_r^B$. The OAM correlations for a particular binary axicon function are shown in Fig. 5(d).

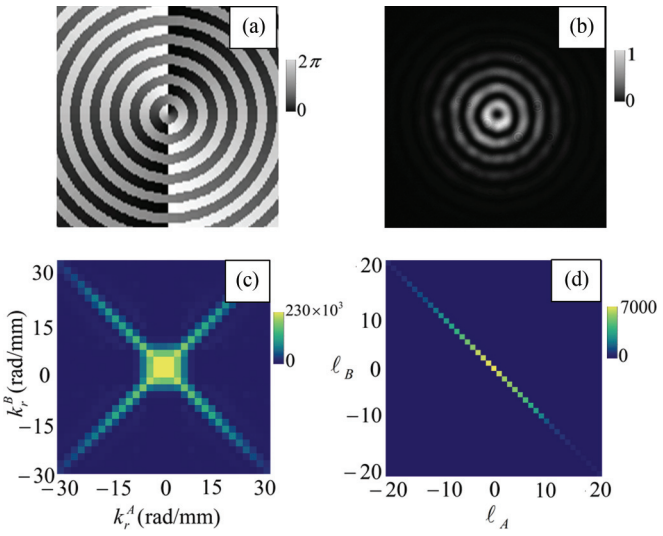

FIG. 5. (Color online) (a) Phase pattern at the plane of the SLM to define a binary axicon of $k_r = 21$ rad/mm and $\ell = 1$. (b) BG beam formed at the plane of the mirror (crystal) by a binary axicon function of $k_r = 21$ rad/mm and $\ell = 1$ with a Gaussian input. (c) Density plot of the single count rates measured in back-projection for different binary axicon phase patterns; varying k_r with $\ell = 0$. The photons from SLM A assume a value of either positive or negative k_r from the binary function. SLM B was encoded with the same function, which allowed BG modes of either positive or negative radial wave vectors to be converted to a Gaussian mode. (d) Density plot of the single count rates measured in back-projection for a particular binary axicon; $k_r = 21$ rad/mm and varying ℓ.

C. Binary Bessel function

The implementation of the binary axicon function confirmed that we indeed measured BG modes. However, the axicon function acts only as an approximation to the Bessel function. Therefore, the final phase pattern considered was that of a binary Bessel function:

$$T_3(r,\phi) = \mathrm{sgn}\{\mathrm{J}_\ell(k_r r)\}\exp(i\ell\phi). \tag{14}$$

Here $\mathrm{J}_\ell(\cdot)$ is the Bessel function of the first kind. Although very similar to the binary axicon function, Eq. (14) provides a more accurate description of an ideal Bessel beam. The spacing between the rings of a Bessel beam generated from an axicon remains constant with the radial position, while the spaces of a theoretical Bessel beam vary in size as we move radially outward from the center, and subsequently depend on k_r. The phase pattern and CCD image of a binary Bessel function are shown in Fig. 6.

A measurable count rate is again obtained along the diagonal where $k_r^A = \pm k_r^B$. However, the off-diagonal crosstalk is now less prominent, compared with Fig. 5(c), particularly surrounding $k_r^{A,B} = 0$. We have generated a BG mode with a better radial approximation, thus creating less overlap between

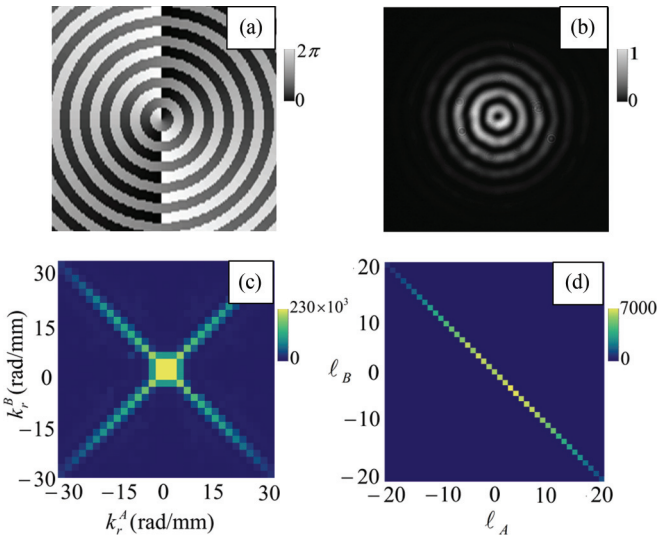

FIG. 6. (Color online) (a) Phase pattern at the plane of the SLM to define a binary Bessel function of $k_r = 21$ rad/mm and $\ell = 1$. (b) BG beam formed at the plane of the mirror (crystal) by a binary Bessel function of $k_r = 21$ rad/mm and $\ell = 1$ with a Gaussian input. (c) Density plot of the single count rates measured in back-projection for different binary Bessel phase patterns; varying k_r with $\ell = 0$. (d) Density plot of the single count rates measured in back-projection for a particular binary Bessel function; $k_r = 21$ rad/mm and varying ℓ.

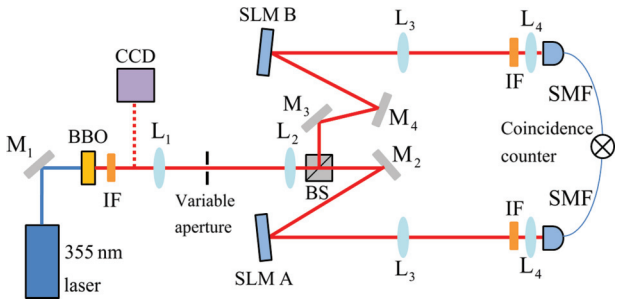

FIG. 7. (Color online) Experimental setup used to detect the OAM eigenstate after SPDC. The plane of the crystal was relay imaged onto two separate SLMs using lenses, L_1 and L_2 ($f_1 = 200$ mm and $f_2 = 400$ mm), where the BG modes were selected. Lenses L_3 and L_4 ($f_3 = 500$ mm and $f_4 = 2$ mm) were used to relay image the SLM planes through 10-nm-bandwidth interference filters (IF) to the inputs of the single-mode fibers (SMF).

the different radial wave vectors. The OAM correlations for a particular binary Bessel function are shown in Fig. 6(d).

V. DOWN-CONVERSION EXPERIMENT AND RESULTS

In SPDC, a nonlinear crystal pumped with a laser beam generates pairs of entangled photons, which are then separately detected. Our SPDC setup is shown in Fig. 7. A mode-locked laser source (Gaussian mode) with a wavelength of 355 nm and an average power of 350 mW was used to pump a 3-mm-thick type I BBO crystal to produce collinear, degenerate entangled photon pairs via SPDC. Using a $4f$ telescope, the plane of the crystal was imaged ($2\times$) onto two separate SLMs which were encoded with the BG transmission functions. The SLM planes were reimaged ($0.4\times$) by a $4f$ telescope and coupled into single-mode fibers, which support only the fundamental Gaussian mode. The fibers were connected to avalanche photodiodes, the outputs of which were connected to a circuit that gives the coincidence count rate. A comparison was made between the back-projected and the down-converted measurements, where we observe that the two methods produce almost-identical results for both the radial and the azimuthal correlations (see Fig. 8). Thus, back-projection provides an effective method with which to qualitatively predict the down-conversion measurements. Ideally, back-projection could be used as a simple technique to fully align the down-conversion system by reflecting the back-projected light off the crystal. However, typically the nonlinear crystal is cut in such a way that requires a slight additional vertical tilt to achieve the phase-matching conditions for collinear down-conversion [28]. This minute change to the crystal orientation is significant enough to misalign the back-projected beam (i.e., the reflected light does not couple into the other fiber). Thus while we achieved good agreement between the back-projected and the down-converted results, we are unable to provide a full quantitative comparison.

The OAM bandwidth (also referred to as the spiral bandwidth) was measured as a function of the different BG phase patterns and compared with the spiral bandwidth measured in the helical basis. Due to conservation of angular momentum

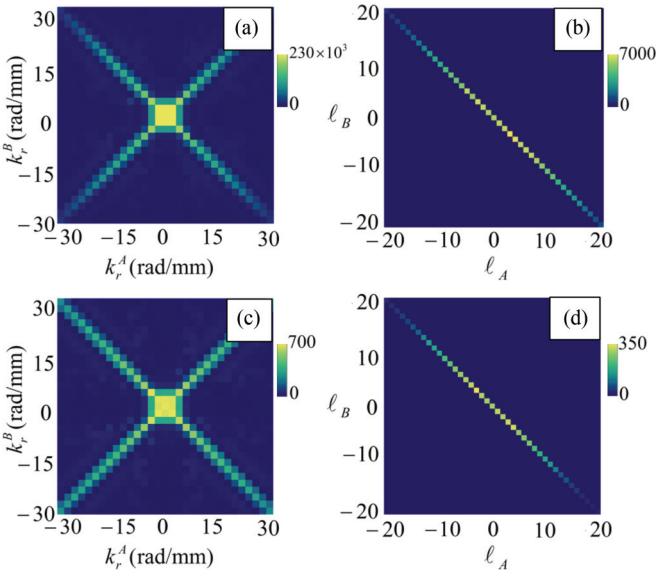

FIG. 8. (Color online) Comparison of the measurements recorded in back-projection (a), (b) with those taken in the down-conversion mode (c), (d). Density plots (a) and (c) both illustrate similar patterns for the measurements taken with $\ell = 0$ and varying k_r. OAM correlations are displayed in (b) and (d) for $k_r = 21$ rad/mm.

[8], a coincidence can only be observed for $\ell_A + \ell_B = 0$, where ℓ_A and ℓ_B are the azimuthal indices of the functions encoded in SLM A and B, respectively. These results are shown in Fig. 9.

The inefficiency of the binary phase pattern results in a decrease in the count rate for both binary phase patterns. Our results show that the binary Bessel phase pattern produces the largest full-width-half-maximum (FWHM) value of 21. The binary axicon function gave an FWHM value of 17, while both the blazed axicon and the vortex functions produced

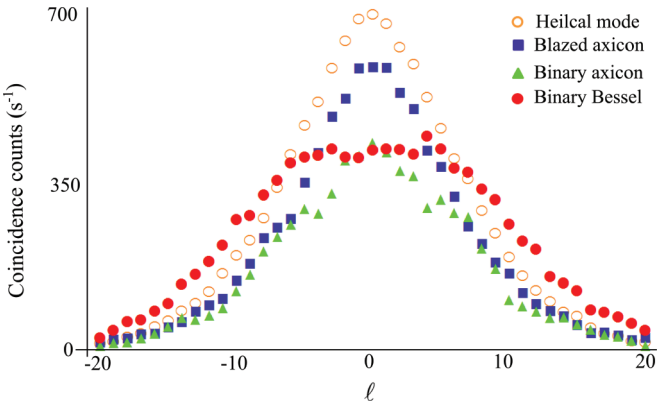

FIG. 9. (Color online) Graph of the measured coincidence count rate as a function of the OAM for four measurement schemes. BG measurements were all measured for $k_r = 21$ rad/mm. Open (orange) circles represent measurements recorded for helical modes. Filled (blue) squares represent measurements recorded using a blazed axicon function. The binary axicon function is represented by filled (green) triangles and measurements from the binary Bessel function are illustrated by filled (red) circles.

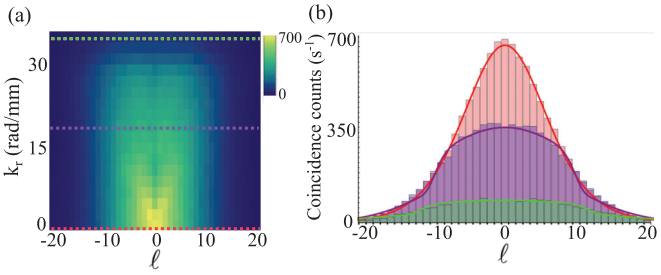

FIG. 10. (Color online) (a) Density plot of the modal spectrum in the BG basis for k_r and ℓ. The efficiency of the coincidence count rate decreases as k_r, however, the FWHM of the bandwidth increases with k_r, shown more clearly in (b). Colored dashed lines in (a) correspond to the profiles plotted in (b) for $k_r = 0$ rad/mm [upper (red) shading], $k_r = 21$ rad/mm [central(purple) shading], and $k_r = 35$ rad/mm [lower (green) shading].

OAM spectra with FWHM values of 15. These graphs were all measured for the particular value of $k_r = 21$ rad/mm.

In investigating the effect of the radial wave vector on the bandwidth, we focused only on the binary Bessel function. We have previously demonstrated [17] proof of entanglement of such beams, where we have shown a violation of Bell's inequality with the Bell parameter $S = 2.78 \pm 0.05$ for the BG subspace of $\ell = 1$.

We now illustrate the broadening and flattening of the OAM spectra in the BG basis, as shown in Fig. 10. We note that the broadening of the OAM spectrum is at the expense of reducing the coincidence counts at low ℓ values. This in turn decreases the heralding efficiency, which has an effect on the security of quantum key distributions. We found, due to the spatial resolution of the SLMs, that there was a maximum limit for which k_r could be chosen. We therefore varied the radial wave vector from 0 to 35 rad/mm. We compare the data in Fig. 10 to the theoretical Schmidt number of Eq. (8). In the case of BG modes, the azimuthal Schmidt number is dependent on the value of the radial wave vector, as shown in Fig. 11. Experimental results are plotted together with a theoretical prediction based on Eqs. (8) and (10) for a collinear SPDC setup ($\omega_0 = 0.50$ mm, $\omega_1 = 0.23$ mm). It is clear that as the value of the radial wave vector increases, so too does the Schmidt number. These results are reminiscent of entanglement concentration, where maximally entangled states are extracted from non–maximally entangled pure states [29]. The increase in accessible OAM modes is advantageous

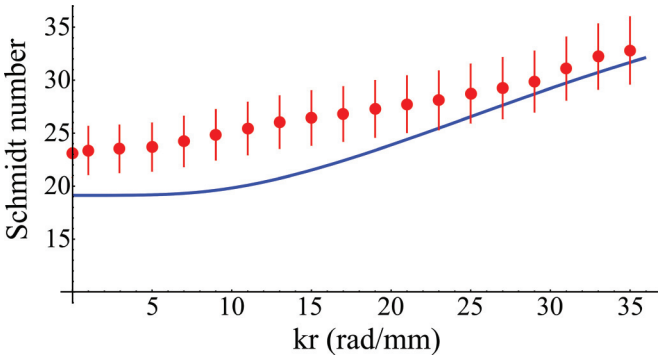

FIG. 11. (Color online) Effect of the radial wave vector on the Schmidt number. For $k_r = 0$, the transmission function corresponds to that of a vortex mode. An increase in the number of available OAM modes is observed as the radial component is increased. Experimental measurements [(red) circles] together with a theoretical prediction [solid (blue) line] are plotted for $\omega_0 = 0.5$ mm and $\omega_1 = 0.23$ mm.

for high-dimensional entanglement, hence offering realizable applications in quantum information processing.

VI. CONCLUSION

We have used back-projection as an aid in designing a measurement scheme for probing OAM correlations. By propagating a classical beam from one of the detectors onto the plane of the crystal, we were able to examine three transmission functions for generating and measuring modes with both helical and radial structures. We investigated the efficacy of a blazed axicon, a binary axicon, and a binary Bessel function in generating BG modes. Only the binary Bessel function resulted in BG modes at the plane of the crystal. OAM correlations in photons generated via SPDC were then measured using these three transmission functions. The OAM bandwidth obtained from the use of both the blazed and the binary axicon transmission functions were similar to the OAM bandwidth obtained when using spiral phase masks, which measure helical modes. However, using the binary Bessel transmission function to measure BG modes leads to a larger OAM bandwidth and more usable OAM modes. The number of modes was shown to increase in a tunable manner, with the minimum set by the LG case. This is useful for quantum information and communication applications requiring entanglement in higher dimensions.

[1] T. B. Pittman, Y. H. Shih, D. V. Strekalov, and A. V. Sergienko, Phys. Rev. A **52**, R3429 (1995).
[2] A. K. Ekert, Phys. Rev. Lett. **67**, 661 (1991).
[3] N. Gisin, G. Ribordy, W. Tittel, and H. Zbinden, Rev. Mod. Phys. **74**, 145 (2002).
[4] M. A. Nielsen and I. L. Chuang, *Quantum Computation and Quantum Information* (Cambridge University Press, Cambridge, UK, 2000).
[5] L. Allen, M. W. Beijersbergen, R. J. C. Spreeuw, and J. P. Woerdman, Phys. Rev. A **45**, 8185 (1992).
[6] H. H. Arnaut and G. A. Barbosa, Phys. Rev. Lett. **85**, 286 (2000).
[7] S. Franke-Arnold, S. M. Barnett, M. J. Padgett, and L. Allen, Phys. Rev. A **65**, 033823 (2002).
[8] A. Mair, A. Vaziri, G. Weihs, and A. Zeilinger, Nature **412**, 313 (2001).
[9] V. Arrizón, Opt. Lett. **28**, 2521 (2003).
[10] C. K. Law and J. H. Eberly, Phys. Rev. Lett. **92**, 127903 (2004).
[11] F. M. Miatto, A. M. Yao, and S. M. Barnett, Phys. Rev. A **83**, 033816 (2011).

[12] V. D. Salakhutdinov, E. R. Eliel, and W. Löffler, Phys. Rev. Lett. **108**, 173604 (2012).
[13] J. P. Torres, A. Alexandrescu, and L. Torner, Phys. Rev. A **68**, 050301 (2003).
[14] J. Durnin, J. Opt. Soc. Am. A **4**, 651 (1987).
[15] J. Durnin, J. J. Miceli, Jr., and J. H. Eberly, Phys. Rev. Lett. **58**, 1499 (1987).
[16] F. Gori, G. Guattari, and C. Padovani, Opt. Commun. **64**, 491 (1987).
[17] M. McLaren, M. Agnew, J. Leach, F. S. Roux, M. J. Padgett, R. W. Boyd, and A. Forbes, Opt. Express **20**, 23589 (2012).
[18] H. Cruz-Ramírez, R. Ramírez-Alarcón, F. J. Morelos, P. A. Quinto-Su, J. C. Gutiérrez-Vega, and A. B. Uŕen, Opt. Express **20**, 29761 (2012).
[19] M. Abramowitz and I. A. Stegun, *Handbook of Mathematical Functions* (Dover, New York, 1972).
[20] F. M. Miatto, D. Giovannini, J. Romero, S. Franke-Arnold, S. M. Barnett, and M. J. Padgett, Eur. Phys. J. D **66**, 178 (2012).
[21] T. B. Pittman, D. V. Strekalov, D. N. Klyshko, M. H. Rubin, A. V. Sergienko, and Y. H. Shih, Phys. Rev. A **53**, 2804 (1996).
[22] S. M. Barnett, D. T. Pegg, J. Jeffers, and O. Jedrkiewicz, Phys. Rev. Lett. **86**, 2455 (2001).
[23] E. K. Tan, J. Jeffers, S. M. Barnett, and D. T. Pegg, Eur. Phys. J. D **22**, 495 (2003).
[24] S. S. R. Oemrawsingh, J. A. de Jong, X. Ma, A. Aiello, E. R. Eliel, G. W. 't Hooft, and J. P. Woerdman, Phys. Rev. A **73**, 032339 (2006).
[25] D. Klyshko, Sov. Phys. Usp. **31**, 74 (1988).
[26] B. Jack, J. Leach, H. Ritsch, S. Barnett, and M. Padgett, New J. Phys. **811**, 103024 (2009).
[27] J. Turunen, A. Vasara, and A. T. Friber, Appl. Opt. **27**, 3959 (1988).
[28] J. Romero, D. Giovannini, S. Franke-Arnold, S. M. Barnett, and M. J. Padgett, Phys. Rev. A **86**, 012334 (2012).
[29] A. Vaziri, J. W. Pan, T. Jennewein, G. Weihs, and A. Zeilinger, Phys. Rev. Lett. **91**, 227902 (2003).